Nodal Brillouin-zone boundary from folding a Chern insulator

Li-Jun Lang,[1,2] Shao-Liang Zhang,[1,3] and Qi Zhou[1,4,*]

[1]*Department of Physics, The Chinese University of Hong Kong, Shatin, New Territories, Hong Kong*

[2]*Division of Physics and Applied Physics, School of Physical and Mathematical Sciences, Nanyang Technological University, Singapore 637371, Singapore*

[3]*School of Physics, Huazhong University of Science and Technology, Wuhan 430074, China*

[4]*Department of Physics and Astronomy, Purdue University, West Lafayette, Indiana 47906, USA*

(Received 1 August 2016; revised manuscript received 26 January 2017; published 16 May 2017)

A Chern insulator is a building block of many topological quantum matters. Here, we discuss a nonsymmorphic Chern insulator, which preserves the nonsymmorphic symmetry and breaks the time-reversal symmetry. It consists of two half-filled Chern insulators, and the bulk energy spectrum is obtained from folding that of either Chern insulator. Such folding gives rise to a nodal boundary of the Brillouin zone, which is protected by the nonsymmorphic symmetries and other lattice symmetries of the system. It also provides one a natural platform to explore the non-Abelian Berry curvature and the resultant quantum phenomena. Moreover, the interplay between nonsymmorphic symmetries and the broken time-reversal symmetry leads to intriguing properties absent in ordinary Chern insulators. An additional degree of freedom, the parity of the nonsymmorphic symmetry, needs to be introduced for describing the topological pumping.

DOI: 10.1103/PhysRevA.95.053615

In the band structure of a crystal, if different bands are separated by finite gaps, a Chern number [1], which is the integral of the Berry curvature in the Brillouin zone (BZ), can be assigned to each individual band. A Chern insulator [2] arises if filling electrons to these bands leads to a finite total Chern number. Such Chern insulators are fundamental elements of a wide range of topological quantum matters, including quantum spin Hall insulators and fractional Chern insulators [3–13].

The study of topological matters using ultracold atoms has been growing fast recently [14,15]. A number of fundamentally important models have been realized, such as the Harper-Hofstadter model [16,17] and the Haldane model [18]. Meanwhile, many topological quantities or phenomena, which are difficult to trace in solids, have been directly observed, such as the Zak phase, Chern numbers [19,20], and topological charge pumping [21,22]. It is promising that ultracold atoms may allow physicists to access new quantum topological states and phenomena.

In this paper, we study a nonsymmorphic Chern insulator, which arises in lattices with nonsymmorphic symmetries and broken time-reversal symmetry. As a fundamental symmetry in solids, nonsymmorphic symmetry has recently attracted extensive interests in the study of topological crystalline matters. It is well known that such symmetry requires that band crossings exist in the band structure. Furthermore, the combination of nonsymmorphic symmetry and other lattice symmetries gives rise to nodal points or nodal lines at certain high-symmetry points [23–27]. So far, these studies have been mainly focusing on systems with time-reversal symmetry. Here, we show that, when the time-reversal symmetry is broken, a nonsymmorphic Chern insulator emerges and exhibits a variety of intriguing properties that are absent in either ordinary Chern insulators or other nonsymmorphic systems that preserve the time-reversal symmetry.

A nonsymmorphic Chern insulator consists of two ordinary insulators, each of which is only half filled. Its band structure can be obtained from folding either of these two ordinary Chern insulators with enlarged BZs. As a result of the folding, energy bands form pairs and cross at the whole BZ boundary. Such a nodal boundary is protected by a nonsymmorphic symmetry, which is a combination of shifting the lattice by half of the lattice spacing and a rotation of the spin, and another symmetry, which is a combination of a mirror reflection and spin flipping. Because of the band-gap crossings at the BZ boundary, the Abelian Berry curvature characterizing conventional Chern insulators is no longer applicable here. It is non-Abelian Berry curvatures from both bands that give rise to a total Chern number of 1 of the system. Thus, this system allows one to explore quantum dynamics controlled by non-Abelian Berry connections and the Wilson line [28]. Whereas the bulk properties are readily rich, edge states of a finite system are even more interesting. Distinct from an ordinary Chern insulator, if the edge respects nonsymmorphic symmetry, the topological pumping, a fundamental phenomenon in topological quantum matters, acquires a new degree of freedom, the parity of the nonsymmorphic symmetry, in addition to charge.

I. THE MODEL AND ITS REALIZATION

Whereas our results are general and can be applied to generic systems with nonsymmorphic symmetry but no time-reversal symmetry, to concretize discussions, we consider a two-dimensional (2D) tight-binding model here. The Hamiltonian reads

$$\hat{H} = \sum_{\langle \mathbf{m}\mathbf{m}'\rangle\sigma} (t\hat{a}^{\dagger}_{\mathbf{m}\sigma}\hat{b}_{\mathbf{m}'\sigma} + t' e^{i\phi_{\mathbf{m}'\sigma}}\hat{a}^{\dagger}_{\mathbf{m}\sigma}\hat{b}_{\mathbf{m}'\bar{\sigma}} + \text{H.c.}) + \sum_{\mathbf{m}\sigma} \eta_{\sigma} m_z (\hat{a}^{\dagger}_{\mathbf{m}\sigma}\hat{a}_{\mathbf{m}\sigma} + \hat{b}^{\dagger}_{\mathbf{m}\sigma}\hat{b}_{\mathbf{m}\sigma}), \quad (1)$$

*qizhou@phy.cuhk.edu.hk

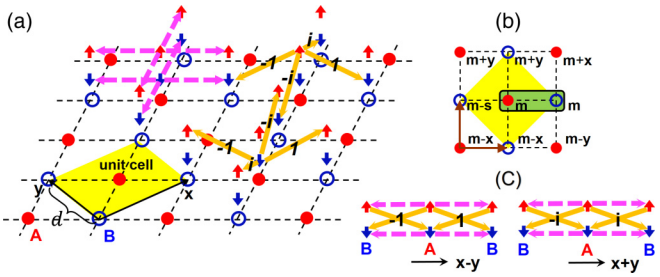

FIG. 1. (a) Solid red and open blue circles represent A and B sublattices, respectively. Dashed pink and solid orange thick arrows represent intra- and inter-spin tunnelings t and t', respectively. (b) $\mathbf{m}$ represents the coordinates of the A site, the four nearest-neighbor B sites $\mathbf{m}'$ of which are denoted as $\mathbf{m}$, $\mathbf{m}-\mathbf{s}$, $\mathbf{m}+\mathbf{y}$, and $\mathbf{m}-\mathbf{x}$. The basis is highlighted by the bold green rectangle. Solid brown arrows represent the spatial part of the nonsymmorphic transformation $G_{x\pm y}$. (c) Schematic of tunnelings along $\hat{x}\mp\hat{y}$ directions. In (a,c), the shaded yellow rhombi highlight the unit cell, and ±1 and $\pm i$ denote the phase factor $e^{i\phi_{\mathbf{m}'\sigma}}$ along different directions.

where $\hat{a}^{(\dagger)}_{\mathbf{m}\sigma}$ and $\hat{b}^{(\dagger)}_{\mathbf{m}\sigma}$ are annihilation (creation) operators for spin-σ ($\sigma=\uparrow,\downarrow$) at A and B sublattice sites $\mathbf{m}$, respectively. $\bar{\sigma}$ represents the inverse of σ. Terms in the first line represent intra- and inter-spin tunnelings t and t' between the nearest-neighbor sites, denoted by $\langle\mathbf{m}\mathbf{m}'\rangle$, as shown in Fig. 1. The phase $\phi_{\mathbf{m}'\sigma}$ depends on the nearest-neighbor site $\mathbf{m}'$ and the spin σ, as shown in Fig. 1(a). Because of these complex tunnelings, $\hat{H}$ does not preserve the time-reversal symmetry. Terms in the second line represent the Zeeman energy m_z, where $\eta_\sigma=1$ and -1 for $\sigma=\uparrow$ and $\downarrow$, respectively. The Hamiltonian in momentum space is $\hat{H}_{\mathbf{k}}=\hat{\Psi}^\dagger_{\mathbf{k}}H(\mathbf{k})\hat{\Psi}_{\mathbf{k}}$ with $\hat{\Psi}^\dagger_{\mathbf{k}}=(\hat{a}^\dagger_{\mathbf{k}\uparrow},\hat{b}^\dagger_{\mathbf{k}\uparrow},\hat{a}^\dagger_{\mathbf{k}\downarrow},\hat{b}^\dagger_{\mathbf{k}\downarrow})$ and

$$H(\mathbf{k})=\begin{pmatrix} m_z & \Omega_{\mathbf{k}}e^{i\theta_{\mathbf{k}}} & 0 & N_{\mathbf{k}}e^{i\theta_{\mathbf{k}}} \\ \Omega_{\mathbf{k}}e^{-i\theta_{\mathbf{k}}} & m_z & -N_{\mathbf{k}}e^{-i\theta_{\mathbf{k}}} & 0 \\ 0 & -N^*_{\mathbf{k}}e^{i\theta_{\mathbf{k}}} & -m_z & \Omega_{\mathbf{k}}e^{i\theta_{\mathbf{k}}} \\ N^*_{\mathbf{k}}e^{-i\theta_{\mathbf{k}}} & 0 & \Omega_{\mathbf{k}}e^{-i\theta_{\mathbf{k}}} & -m_z \end{pmatrix}, \quad (2)$$

where $\Omega_{\mathbf{k}}=2t[\cos\frac{(k_x-k_y)d}{2}+\cos\frac{(k_x+k_y)d}{2}]$, $N_{\mathbf{k}}=2t'[i\sin\frac{(k_x-k_y)d}{2}+\sin\frac{(k_x+k_y)d}{2}]$, and $\theta_{\mathbf{k}}=\frac{(k_y-k_x)d}{2}$. $H(\mathbf{k})$ can be block-diagonalized to $\hat{H}_{\mathbf{k}}=\hat{\Phi}^\dagger_{\mathbf{k}}\tilde{H}(\mathbf{k})\hat{\Phi}_{\mathbf{k}}$ with $\hat{\Phi}^\dagger_{\mathbf{k}}=(\hat{s}^\dagger_{\mathbf{k},+},\hat{p}^\dagger_{\mathbf{k},+},\hat{s}^\dagger_{\mathbf{k}-},\hat{p}^\dagger_{\mathbf{k},-})$ and $\hat{s}^\dagger_{\mathbf{k},\pm}=\frac{1}{\sqrt{2}}(\hat{a}^\dagger_{\mathbf{k},\uparrow}\pm e^{-i\theta_{\mathbf{k}}}\hat{b}^\dagger_{\mathbf{k},\uparrow})$, $\hat{p}^\dagger_{\mathbf{k},\pm}=\frac{1}{\sqrt{2}}(\hat{a}^\dagger_{\mathbf{k},\downarrow}\mp e^{-i\theta_{\mathbf{k}}}\hat{b}^\dagger_{\mathbf{k},\downarrow})$, and

$$\tilde{H}(\mathbf{k})=\begin{pmatrix} H_+(\mathbf{k}) & 0 \\ 0 & H_-(\mathbf{k}) \end{pmatrix}, \quad (3)$$

where $H_\pm(\mathbf{k})\equiv(m_z\pm\Omega_{\mathbf{k}})\sigma_z\mp\mathrm{Re}(N_{\mathbf{k}})\sigma_x\pm\mathrm{Im}(N_{\mathbf{k}})\sigma_y$ with $\sigma_{x,y,z}$ being the Pauli matrices are standard Hamiltonians of Chern insulators with Chern number 1. The BZ of $H_\pm(\mathbf{k})$ doubles that of $H(\mathbf{k})$, and $H_+(\mathbf{k})=H_-(\mathbf{k}+\mathbf{G})$ with $\mathbf{G}$ being the reciprocal-lattice vector of $H(\mathbf{k})$. This shows that our system consists of two Chern insulators. The band structure can be viewed as folding that of either. In addition, as $SH^*_\pm(-k_x,k_y)S^\dagger=S^\dagger H^*_\pm(k_x,-k_y)S=H_\pm(\mathbf{k})$, where $S=\mathrm{diag}(1,i)$, both $H_+(\frac{\pi}{d},k_y)=H_-(\frac{\pi}{d},k_y)$ and $H_+(k_x,\frac{\pi}{d})=H_-(k_x,\frac{\pi}{d})$ are satisfied, and band crossing occurs through the whole BZ boundary, as shown in Fig. 2. Such folding can also

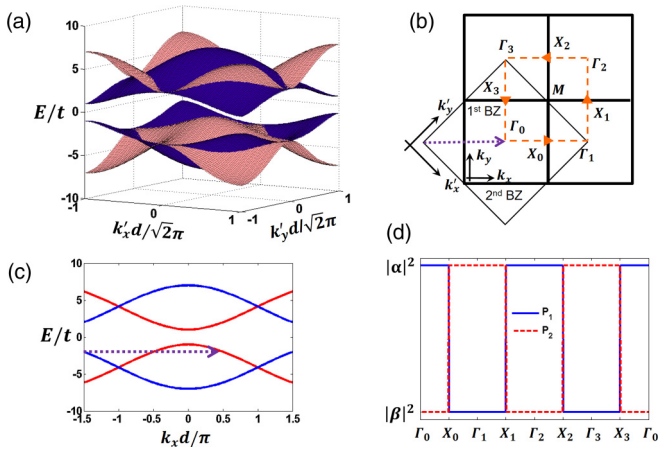

FIG. 2. (a) The band structure of $H(\mathbf{k})$ contains those from two Chern insulators $H_+(\mathbf{k})$ (pink or light gray) and $H_-(\mathbf{k})$ (blue or dark gray), which cross at the BZ boundary. (b) BZ of $H(\mathbf{k})$. The bold frame represents the nodal boundary. Γ_0 is the center of the first BZ, and $\Gamma_{1,2,3}$ are its equivalent points. (c) The energy spectrum along $k_y=0$. Dotted purple arrows in (b,c) denote the folding by a reciprocal-lattice vector $\mathbf{G}$. (d) Probabilities of the final state in first and second bands, P_1 (solid blue line) and P_2 (dashed red line) along the loop denoted by the dashed orange line in (b), if the initial state is prepared as $\eta_{\mathbf{k}_i}=(\alpha,\beta)^T$. Here we use the tight-binding parameters as $t'=t, m_z=-3t$.

be seen from the real space (Appendix A). Unlike the ordinary nodal lines or rings in other systems [25–27,29,30], here we have a nodal boundary enclosing the whole BZ. Figure 2(a) also shows that the lowest two bands of $H(\mathbf{k})$ in the first BZ are contributed by $H_+(\mathbf{k})$ and $H_-(\mathbf{k})$, respectively. For a band insulator with half filling, both the lowest bands of $H_\pm(\mathbf{k})$ are only half filled. This insulator is thus formed by assembling two half-filled Chern insulators in momentum space.

Equation (1) can be realized by multiple schemes in ultracold atoms. Here we focus on one scheme that has been realized in experiments [31]. The Hamiltonian reads

$$H(\mathbf{r})=\left[\frac{\mathbf{p}^2}{2M}+V(\mathbf{r})\right]\sigma_0+\Omega_x(\mathbf{r})\sigma_x+\Omega_y(\mathbf{r})\sigma_y+m_z\sigma_z, \quad (4)$$

where $V(\mathbf{r})=V[\cos^2\frac{\pi(x-y)}{d}+\cos^2\frac{\pi(x+y)}{d}]$ is a spin-independent square lattice potential with lattice spacing $d/\sqrt{2}$, and $\Omega_{x,y}(\mathbf{r})=\pm\Omega\cos\frac{\pi(x\mp y)}{d}\sin\frac{\pi(x\pm y)}{d}$ are the Raman potentials, which double the unit cell of $V(\mathbf{r})$. In the limit where the Raman coupling strength Ω is much weaker than the gap between s and p bands of $V(\mathbf{r})$, the band structure and topological properties of the system are well captured by Eq. (1). In Ref. [31], although Eq. (4) was produced, it just explored half of the four bands in the first BZ. The nodal BZ boundary and the resultant non-Abelian topological properties were not studied. Also, to measure the Chern number, a proper method based on non-Abelian Berry curvature should be used, as discussed below. An alternative experimental scheme is presented in Appendix B.

The existence of the nodal boundary can also be understood from the symmetry. Two nonsymmorphic symmetry operators are defined as $G_{x\pm y}=T_{\hat{x}}(\frac{d}{2})T_{\hat{y}}(\pm\frac{d}{2})R_{\frac{\pi}{2}}$, where $T_{\hat{x}(\hat{y})}(l)$ is a

translation along the $x(y)$ direction for a distance l, and $R_{\frac{\pi}{2}} = e^{-i\frac{\pi}{2}\sigma_z}$ is a spin rotation about the z axis for π. These two operators are related to each other by $G_{x+y} = G_{x-y}T_{\hat{y}}(d)$. Nonsymmorphic crystalline symmetry has been considered in a variety of systems [23–27,32–34]. Here, we have such symmetries along two directions. Since $G^2_{x\pm y}$ has eigenvalue $-e^{i(k_x\pm k_y)d}$, the eigenvalues of $G_{x\pm y}$ should be $ie^{i(k_x\pm k_y)d/2}$ or $-ie^{i(k_x\pm k_y)d/2}$. As $2\pi/d$ change of either k_x or k_y inverses the sign of the eigenvalues of $G_{x\pm y}$, there must be band crossing in the BZ. Moreover, there are two additional symmetries, M_x—$x \to -x$, $\sigma_x \leftrightarrow \sigma_y$—and M_y—$y \to -y$, $\sigma_x \leftrightarrow -\sigma_y$. Following the argument in Ref. [33], such band crossing must occur at the BZ boundary, since $G_{x+y}(G_{x-y})$ and $M_x(M_y)$ are anticommutative at $k_x(k_y) = \pm\pi/d$. The system thus has a double degeneracy at the BZ boundary, i.e., a nodal boundary enclosing the first BZ. As $G_{x+y} = G_{x-y}T_{\hat{y}}(d)$, the parity λ of the nonsymmorphic symmetry can be defined as the sign of the eigenvalues of $G_{x\pm y}$. When $m_z/t > 0$, the Bloch functions of the lowest two bands have $\lambda = +$ and $-$, respectively. It is worth mentioning that the difference between them is measurable (Appendix C).

II. NON-ABELIAN BERRY CURVATURE AND WILSON LOOP

Due to the nodal boundary, Abelian Berry curvature is no longer applicable, and the non-Abelian one is inevitably required. If $w \ll \Delta$, where w is the total bandwidth of the lowest two bands and Δ is the gap between the second and the third bands, the lowest two bands are nearly degenerate and the highest two can be ignored. Non-Abelian Berry curvature is defined as $\mathbf{F} = \nabla_{\mathbf{k}} \times \mathbf{A} - i\mathbf{A} \times \mathbf{A}$, where $\mathbf{A}^{nm} = i\langle u^n_{\mathbf{k}}|\nabla_{\mathbf{k}}|u^m_{\mathbf{k}}\rangle$ is the non-Abelian Berry connection with $|u^n_{\mathbf{k}}\rangle$ being the periodic Bloch state for the nth band [4]. It determines the dynamics of wave packets uploaded to the system [35]. Preparing an atomic cloud, say, a Bose-Einstein condensate at an initial momentum $\mathbf{k}_i$, and applying an external force $\mathbf{F}_{\text{ext}}$, the strength of which satisfies $w \ll |\mathbf{F}_{\text{ext}}|d \ll \Delta$, the dynamics is dominated by the lowest two bands. We define the wave packet as $|w\rangle = \sum_{\mathbf{k}}(\alpha_{\mathbf{k}}|\psi^1_{\mathbf{k}}\rangle + \beta_{\mathbf{k}}|\psi^2_{\mathbf{k}}\rangle)$, where $|\psi^n_{\mathbf{k}}\rangle$ is the Bloch state for the nth band, and $\eta_{\mathbf{k}} = (\alpha_{\mathbf{k}}, \beta_{\mathbf{k}})^T$ with $|\alpha_{\mathbf{k}}|^2 + |\beta_{\mathbf{k}}|^2 = 1$ can be regarded as a pseudospin. For simplicity, we assume a delta function wave packet in momentum space, the semiclassical dynamics of which is determined by [35]

$$\hbar\dot{\mathbf{r}} = \nabla_{\mathbf{k}}\langle w|H_{\mathbf{k}}|w\rangle - \hbar\dot{\mathbf{k}} \times \eta^\dagger_{\mathbf{k}}\mathbf{F}\eta_{\mathbf{k}}, \tag{5}$$

$$\hbar\dot{\mathbf{k}} = \mathbf{F}_{\text{ext}}, \quad i\hbar\dot{\eta}_{\mathbf{k}} = -\hbar\dot{\mathbf{k}} \cdot \mathbf{A}\eta_{\mathbf{k}}, \tag{6}$$

which show that the movement in momentum space is accompanied by rotating the pseudospin $\eta_{\mathbf{k}}$, reflecting the non-Abelian nature of the dynamics.

Equation (6) gives $\eta_{\mathbf{k}_f} = W_{\mathbf{k}_i\to\mathbf{k}_f}\eta_{\mathbf{k}_i}$, where $W_{\mathbf{k}_i\to\mathbf{k}_f} = \mathcal{P}\exp(i\int^{\mathbf{k}_f}_{\mathbf{k}_i}\mathbf{A}\cdot d\mathbf{k})$ is the Wilson line [28] with the path-ordering operator $\mathcal{P}$. If $\eta_{\mathbf{k}_i} = (1,0)^T$ as initial state, $|W_{11}|^2$ and $|W_{21}|^2$ correspond to the probabilities of the final state in the first and second bands, respectively. Tracing $\eta_{\mathbf{k}}$ thus reconstructs the Wilson line, as shown in a recent experiment [36]. For the loop in Fig. 2(b), the step-function-like $|W_{11}|^2$ and $|W_{21}|^2$ in Fig. 2(d) reflect that λ is conserved in the evolution, and the lowest two bands cross at the BZ boundary [34]. The Wilson loop in Fig. 2(b) is explicitly written as

$$W = \begin{pmatrix} e^{i\varphi_-} & 0 \\ 0 & e^{i\varphi_+} \end{pmatrix}, \quad \varphi_+ + \varphi_- = \int_S \text{tr}(\mathbf{F})\cdot d\mathbf{S}, \tag{7}$$

where S denotes the area enclosed by the loop. If S is the whole BZ, the U(1) part of W, $e^{i(\varphi_+ + \varphi_-)/2}$, is related to the Chern number, as shown later. Whereas we have chosen a particular path in the k space, we would like to emphasize that, different from other nodal lines in the BZ, any path shall meet a band crossing point here, due to the nodal BZ boundary. Thus, Wilson lines are always required.

III. CHERN NUMBER AND ANOMALOUS VELOCITY

The last term in Eq. (5) describes the anomalous velocity [4,35]. Considering an insulator with fermions fully filling up the lowest two bands, the anomalous velocity per particle, if setting $\mathbf{F}_{\text{ext}} = f\hat{y}$, can be written as

$$\mathbf{v}_a = -\frac{d^2}{2h} f C\hat{x} \equiv -v_{ax}\hat{x}, \tag{8}$$

where $C = \int_{BZ}\text{tr}(F_z)dk_xdk_y/2\pi$ is the Chern number of the lowest two bands. Equation (8) allows one to experimentally measure the Chern number through the anomalous velocity in the transverse direction of the dragging force, similar to the Abelian case in a recent experiment [20].

$C = 1$ in our system can also be understood from the block-diagonalized Hamiltonian $\tilde{H}(\mathbf{k})$. For each of $H_\pm(\mathbf{k})$, the Chern number can be computed as $C'_\pm = \frac{1}{2\pi}\int_{BZ'} F^\pm_z dk_xdk_y = 1$, where $F^\pm_z$ is the z component of the Abelian Berry curvature of $H_\pm(\mathbf{k})$, and BZ' denotes the BZ of $H_\pm(\mathbf{k})$. Since BZ' doubles the BZ of $H(\mathbf{k})$, $C_\pm = \frac{1}{2\pi}\int_{BZ} F^\pm_z dk_xdk_y$ is not an integer in the first BZ of the system. Nevertheless, because $H_+(\mathbf{k}) = H_-(\mathbf{k}+\mathbf{G})$, one obtains $C_+ + C_- = 1$. This observation shows that, though the Chern number, which controls the contribution to the charge pumping, from each individual Chern insulator is not quantized in a single pumping period, the sum of them gives a well quantized Chern number and thus charge pumping. Interestingly, if one can selectively fill the first and third bands, a quantized pseudospin pumping can be realized (Appendix D). This picture is also useful for understanding the Wilson loop in Eq. (7). As $\lambda = \pm$ is conserved along the loop, in the basis of eigenstates of $H_\pm(\mathbf{k})$, the Wilson loop is diagonal and thus the accumulated phase $\varphi_\pm = 2\pi C_\pm$, the sum of which is indeed the $2\pi C$.

IV. EDGE STATES

The edge states in a nonsymmorphic Chern insulator exhibit much richer physics than an ordinary Chern insulator. We consider the A-B-A edge that respects the nonsymmorphic symmetry. Since the crystal momentum q_y along the edge is a good quantum number, effective one-dimensional (1D) tight-binding models $\hat{h}(q_y)$ can be obtained straightforwardly (Appendix E), which can also be block-diagonalized to

$$\sum_{\nu=\pm}\hat{h}_\nu(q_y) = \sum_{\nu=\pm}(\hat{t}_\nu + \hat{e}_\nu + \hat{v}_\nu), \tag{9}$$

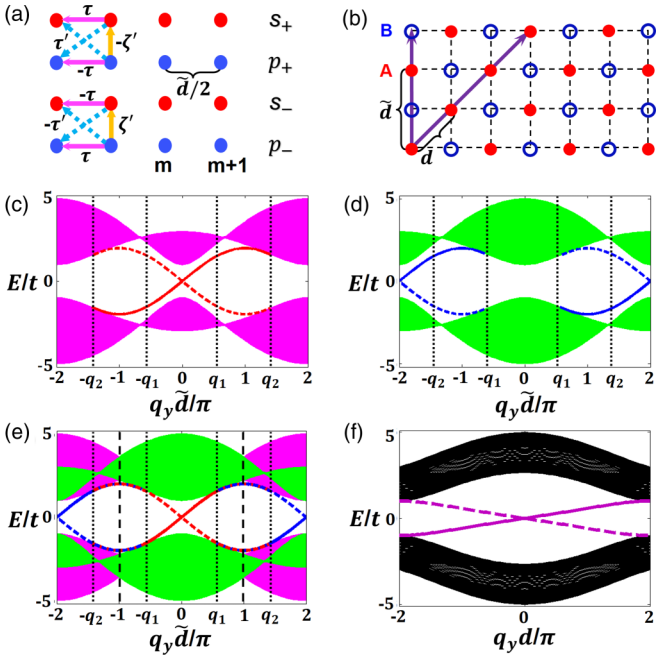

FIG. 3. (a) Schematics of $\hat{h}_{\pm}(q_y)$, with tunnelings defined in the text. (b) A-B-A and A-A-A edges denoted by the arrows. (c,d) Energy spectra of $\hat{h}_{+}(q_y)$ and $\hat{h}_{-}(q_y)$ with parities $+$ and $-$, respectively. (e) Energy spectrum of the realistic system with A-B-A edges, which is contributed from both $\hat{h}_{\pm}(q_y)$. Two dashed vertical lines highlight the first edge BZ. In the region between two dotted vertical lines $q_1 \leqslant |q_y|\tilde{d}/\pi \leqslant q_2$, edge states are doubled at each edge. (f) Energy spectrum of A-A-A edges. In (c–f), the edge states on the right and left boundaries are denoted by solid and dashed lines in the bulk gaps, respectively. Here we use the tight-binding parameters as $t' = -m_z = t$ for calculation.

where

$$\hat{t}_v = v \sum_m [\tau(\hat{s}^\dagger_{vm}\hat{s}_{v,m+1} - \hat{p}^\dagger_{vm}\hat{p}_{v,m+1}) + \text{H.c.}], \quad (10)$$

$$\hat{e}_v = v \sum_m [\tau'(\hat{s}^\dagger_{vm}\hat{p}_{v,m+1} + \hat{p}^\dagger_{vm}\hat{s}_{v,m+1}) - \zeta'\hat{s}^\dagger_{vm}\hat{p}_{vm} + \text{H.c.}], \quad (11)$$

$$\hat{v}_v = (m_z + v\zeta) \sum_m (\hat{s}^\dagger_{vm}\hat{s}_{vm} - \hat{p}^\dagger_{vm}\hat{p}_{vm}), \quad (12)$$

with $\tau = te^{-iq_y\tilde{d}/2}$, $\tau' = it'e^{-iq_y\tilde{d}/2}$, $\zeta = 2t\cos\frac{q_y\tilde{d}}{2}$, and $\zeta' = 2it'\sin\frac{q_y\tilde{d}}{2}$. $\tilde{d} = \sqrt{2}d$ is the lattice spacing along the A-B-A direction, as shown in Fig. 3(b). Each block $\hat{h}_v(q_y)$, in new basis $\hat{s}_v$ and $\hat{p}_v$, represents a 1D hybridized s-p model [37–39], as shown in Fig. 3(a), and may support edge states for certain values of q_y.

The period of $\hat{h}_{\pm}(q_y)$ in q_y doubles that of $\hat{h}(q_y)$. Moreover, $\hat{h}_{+}(q_y + 2\pi/\tilde{d}) = \hat{h}_{-}(q_y)$ as the A-B-A edge respects the nonsymmorphic symmetry. Thus the edge BZ can be regarded as the one folded from that of $\hat{h}_{\pm}(q_y)$, and the edge states also show up in pairs, unless some of them merge into the bulk spectrum, as shown in Fig. 3(e). For comparison, we also show the edge states of the A-A-A edge, which are the same as those of an ordinary Chern insulator, since such an edge breaks the nonsymmorphic symmetry. For the A-B-A edge, there might be one or two edge states, which depends on q_y. For some values of q_y, both $\hat{h}_{+}(q_y)$ and $\hat{h}_{-}(q_y)$ have edge states, whereas for others only one of them contributes. Such a feature of edge states has an interesting consequence in the topological pumping, which has an extra degree of freedom associated with the nonsymmorphic symmetry. As shown in Fig. 4, at $q_y = 0$ an edge state with parity $+$ is initially prepared at the right edge of the system. Increasing q_y, such an edge state gradually merges to the bulk and eventually shows up on the other edge at $q_y = 2\pi/\tilde{d}$. Note that this is only half of the period of $\hat{h}_{\pm}(q_y)$, and neither of them contributes to a quantized charge pumping, but the total contribution is a well quantized one. Moreover, the parity of the edge changes to $-$. When q_y increases from $2\pi/\tilde{d}$ to $4\pi/\tilde{d}$, there is no charge pumping, but the parity changes. Only when q_y reaches $8\pi/\tilde{d}$, the initial edge state revives both in charge and parity. Thus, the parity of nonsymmorphic symmetry emerges as a new degree of freedom in the topological pumping.

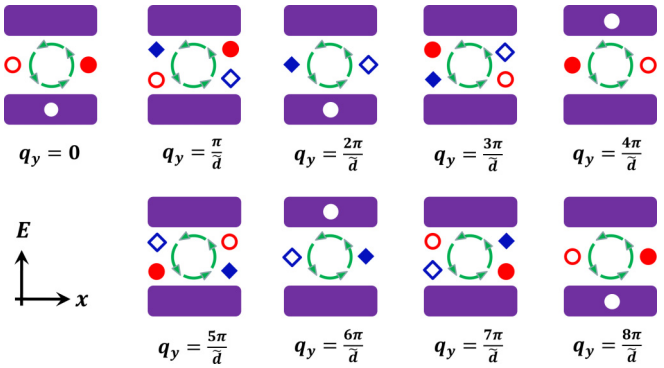

FIG. 4. Schematic of the topological pumping with A-B-A edges. Shaded purple rectangles represent the filled bulk states and the white circle therein means a hole. Solid (open) red circles and blue squares represent filled (unfilled) edge states with the nonsymmorphic parities, $+$ and $-$, respectively. Counterclockwise green arrows represent the pumping direction.

We would like to point out that all our results can be applied to generic nonsymmorphic systems with broken time-reversal symmetry. For instance, we have verified that, if adding a term in the model considered in Ref. [23] to break the time-reversal symmetry, a nonsymmorphic Chern insulator also arises, and all our results apply. We also explore small perturbations to break either nonsymmorphic symmetry or the symmetry $M_{x(y)}$, which do not change the results qualitatively (Appendices F and G).

V. CONCLUSION

The preserved nonsymmorphic symmetry and broken time-reversal symmetry in a nonsymmorphic Chern insulator give rise to a variety of unique properties in both the bulk and the edge, distinct from those of ordinary Chern insulators. We hope that our work will stimulate more studies of non-Abelian topological quantum matters and nonsymmorphic symmetries.

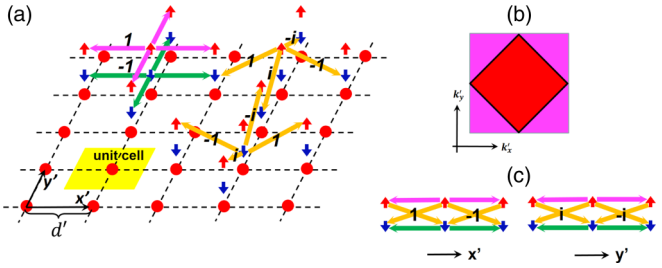

FIG. 5. Folding in real space. (a) Schematics of tunnelings. After the transformation, $b^{\dagger}_{\mathbf{m}\downarrow} \to -b^{\dagger}_{\mathbf{m}\downarrow}$, A and B sublattices in Fig. 1(a) become equivalent, and are thus denoted by red circles uniformly. The intraspin tunnelings have opposite signs for spin up and spin down. A reduced unit cell has been highlighted by the shaded yellow square. Other notations are the same as those of Fig. 1(a). (b) The small red square is the first BZ of the original system, while addition of the pink triangle ones yields the enlarged first BZ of the transformed system. (c) Schematic of the tunnelings along $\hat{x}'$ and $\hat{y}'$ directions, respectively.

ACKNOWLEDGMENTS

This work is supported by Hong Kong Research Grants Council/Collaborative Research Fund (Grant No. HKUST3/CRF/13G) and partially by startup funds for Q.Z. from Purdue University.

L.-J.L. and S.-L.Z. contributed equally to this work.

APPENDIX A: BAND FOLDING BY A TRANSFORMATION IN REAL SPACE

Making a simple transformation, say $b^{\dagger}_{\mathbf{m}\downarrow} \to -b^{\dagger}_{\mathbf{m}\downarrow}$, in real space, the unit cell halves that of the original system Eq. (1), making A and B sublattices equivalent and the lattice spacing $d' = d/\sqrt{2}$, as shown in Fig. 5(a). We thus can uniformly use the annihilation (creation) operator $\hat{c}^{(\dagger)}_{\mathbf{m}\sigma}$ right now, with $\mathbf{m}$ being the coordinates of the lattice site and σ the spin. Correspondingly, the tight-binding Hamiltonian becomes

$$\hat{H} = \sum_{\langle \mathbf{m}\mathbf{m}'\rangle\sigma} (\eta_\sigma t \hat{c}^{\dagger}_{\mathbf{m}\sigma}\hat{c}_{\mathbf{m}'\sigma} - t' e^{i\phi_{\mathbf{m}'\sigma}}\hat{c}^{\dagger}_{\mathbf{m}\sigma}\hat{c}_{\mathbf{m}'\bar{\sigma}} + \text{H.c.}) + \sum_{\mathbf{m}\sigma} \eta_\sigma m_z \hat{c}^{\dagger}_{\mathbf{m}\sigma}\hat{c}_{\mathbf{m}\sigma}, \tag{A1}$$

where $\bar{\sigma}$ represents the inverse of σ. The first sum represents the intra- and inter-spin tunnelings t and t' between the nearest-neighbor sites, denoted by $\langle \mathbf{m}\mathbf{m}'\rangle$. The phase $\phi_{\mathbf{m}'\sigma}$ of the interspin tunneling depends on the nearest-neighbor site $\mathbf{m}'$ and the spin σ, as shown in Fig. 5(a). The second sum represents the Zeeman energy, where $\eta_\sigma = 1$ and -1 for $\sigma = \uparrow$ and $\downarrow$, respectively. The corresponding Hamiltonian in momentum space is $\hat{H} = \sum_{\mathbf{k}} \Psi^{\dagger}_{\mathbf{k}} H(\mathbf{k}) \Psi_{\mathbf{k}}$ with $\Psi^{\dagger}_{\mathbf{k}} = (\hat{c}^{\dagger}_{\mathbf{k}\uparrow}, \hat{c}^{\dagger}_{\mathbf{k}\downarrow})$ and

$$H(\mathbf{k}) = \begin{pmatrix} m_z + \Omega_{\mathbf{k}} & -N_{\mathbf{k}} \\ -N^{*}_{\mathbf{k}} & -m_z - \Omega_{\mathbf{k}} \end{pmatrix}, \tag{A2}$$

where $\Omega_{\mathbf{k}} = 2t(\cos k'_x d' + \cos k'_y d')$, $N_{\mathbf{k}} = 2t' i(\sin k'_x d' + \sin k'_y d')$. For convenience, we use rotated coordinates x' and y', as shown in Fig. 5, and thus define $k'_x = (k_x - k_y)/\sqrt{2}$ and $k'_y = (k_x + k_y)/\sqrt{2}$, correspondingly. Note that Eq. (A2) is just the one block, $H_+(\mathbf{k})$, of the Hamiltonian Eq. (3), and the first Brillouin zone thus doubles the original one, as shown in Fig. 5(b). Alternatively, another transformation, $\hat{b}^{\dagger}_{\mathbf{m}\uparrow} \to -\hat{b}^{\dagger}_{\mathbf{m}\uparrow}$, gives rise to $H_-(\mathbf{k})$. Since these transformations actually halve the unit cell, folding the energy spectrum of either $H_+(\mathbf{k})$ or $H_-(\mathbf{k})$ gives rise to the band structure of the realistic system.

APPENDIX B: AN ALTERNATIVE EXPERIMENTAL SCHEME

By a unitary transformation, $\sigma_x \to \sigma_z$, $\sigma_z \to \sigma_x$, of the Hamiltonian Eq. (4), we get an alternative equivalent Hamiltonian as

$$V(\mathbf{r}) = V_0(\mathbf{r})\sigma_0 + V_s(\mathbf{r})\sigma_z + B_y(\mathbf{r})\sigma_y + B_x\sigma_x, \tag{B1}$$

where Pauli matrices can be regarded as real spins. Using the rotated coordinates $x' = (x - y)/\sqrt{2}$ and $y' = (x + y)/\sqrt{2}$, $V_0(\mathbf{r}) = V(\cos^2\frac{\pi x'}{d'} + \cos^2\frac{\pi y'}{d'})$ is a spin-independent square lattice potential with lattice spacing $d' = d/\sqrt{2}$, and $V_s(\mathbf{r}) = V_s \cos\frac{\pi x'}{d'} \sin\frac{\pi y'}{d'}$ is a spin-dependent potential with lattice spacing d, as shown in Figs. 6(a) and 6(b), respectively. V and V_s are the corresponding potential strengths. The first two terms in Eq. (B1) yield a spin-dependent two-dimensional double-well lattice, along the x' direction of which is an effective one-dimensional double-well lattice, as shown in Fig. 6(c). B_x and $B_y(\mathbf{r}) = B \sin\frac{\pi x'}{d} \cos\frac{\pi y'}{d}$ are the space-

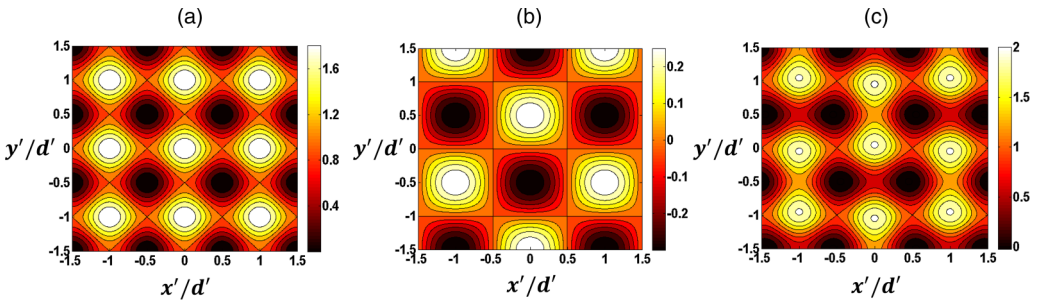

FIG. 6. Potentials in Eq. (B1). (a) The spin-independent square lattice potential, $V_0(\mathbf{r})$, with lattice spacing d', where $V = E_R$, $E_R = \hbar^2 k_0^2/2M, k_0 = \pi/d'$, and M is the atom mass. (b) The spin-dependent potential, $V_s(\mathbf{r})$, with lattice spacing d, where $V_s = 0.3E_R$. (c) The two-dimensional double-well lattice potential, induced by both $V_0(\mathbf{r})$ and $V_s(\mathbf{r})$, where V and V_s are taken as the same values as those in (a) and (b).

independent and -dependent effective magnetic fields along x and y directions, respectively. B is the strength of the magnetic field. If we make $B = V_s$, the model is equivalent to the one we used in the main text, and thus the nodal BZ boundary can be obtained.

APPENDIX C: MEASURING EIGENVALUES OF THE NONSYMMORPHIC OPERATOR

The nonsymmorphic operator G_{x+y} shifts the particle along both the x and y directions for half of the lattice spacing, and meanwhile rotates the spin about the z axis for π. Physically, the eigenvalue of G_{x+y} is the phase difference of the wave function at $\mathbf{R}$ and $\mathbf{R}'$, where $\mathbf{R}$ includes both the real-space coordinate and the spin, and $\mathbf{R} \to \mathbf{R}'$ under G_{x+y}. The standard technique for measuring the single-particle correlation function can then be directly generalized to our system [40,41]. One simply needs to add a π pulse in the spin space in addition to shifting a copy of the sample by half of the lattice spacing.

If one is only interested in the parity of nonsymmorphic symmetry $\lambda = \pm$, a simple Ramsey interferometry can be used. Preparing an initial state $\Psi_i(\mathbf{r}) = [\Psi_{1\mathbf{k}}(\mathbf{r}) + \Psi_{2\mathbf{k}}(\mathbf{r})]/\sqrt{2}$, its evolution with time t yields $\Psi_f(\mathbf{r}) = [\Psi_{1\mathbf{k}}(\mathbf{r}) + e^{-i\omega t}\Psi_{2\mathbf{k}}(\mathbf{r})]/\sqrt{2}$, where $\hbar\omega$ is the energy difference between the lowest two bands at momentum $\mathbf{k}$. Applying a $\pi/2$ pulse and $\Psi_{1\mathbf{k}}(\mathbf{r}) \to [\Psi_{1\mathbf{k}}(\mathbf{r}) + \Psi_{2\mathbf{k}}(\mathbf{r})]/\sqrt{2}$, $\Psi_{2\mathbf{k}}(\mathbf{r}) \to [\Psi_{1\mathbf{k}}(\mathbf{r}) - \Psi_{2\mathbf{k}}(\mathbf{r})]/\sqrt{2}$, one detects the probability of occupying the lowest band as $P(t) = \cos^2(\omega t/2)$. Alternatively, applying the nonsymmorphic operator G_{x-y} to $\Psi_i(\mathbf{r})$, one obtains $\Psi_i'(\mathbf{r}) = ie^{i(k_x-k_y)d/2}[\Psi_{1\mathbf{k}}(\mathbf{r}) - \Psi_{2\mathbf{k}}(\mathbf{r})]/\sqrt{2}$. Such nonsymmorphic operation is directly available by simultaneously shifting the lattice, i.e., changing the relative phase of the lasers, and rotating the spin. One then repeats the previous steps, and the probability becomes $P'(t) = \sin^2(\omega t/2)$. The phase shift between $P'(t)$ and $P(t)$ is a direct consequence of the difference λ between the lowest two bands.

APPENDIX D: QUANTUM PSEUDOSPIN PUMPING

Besides filling up the lowest two bands to get an insulator with Chern number 1 as in the main text, if one could selectively populate different bands, even more interesting phenomena may occur. Now consider filling up the first and the third bands, which corresponds to the ground band of $H_+(\mathbf{k})$ and the excited band of $H_-(\mathbf{k})$, respectively, in Eq. (3). Since the Chern number changes sign in the excited bands, one sees that the net charge pumped, which is given by $C_{+g} + C_{-e} = C_{+g} - C_{-g}$ with $g(e)$ denoting the ground (excited) band, is not quantized in a single pumping period. The charge currents from these two insulators apparently have opposite directions. On the other hand, one notes that $H_+(\mathbf{k})$ and $H_-(\mathbf{k})$ correspond to $\lambda = +$ and $\lambda = -$, respectively, and one could define a parity or pseudospin current as

$$j_s \equiv j_+ - j_- = (C_{+g} - C_{-e})\frac{q^2E}{h} = \frac{q^2E}{h}, \tag{D1}$$

where q is the effective charge of the atom and $E = f/q$ is the effective electric field along the direction of the dragging force f. One thus has a quantized pseudospin pumping.

APPENDIX E: DIMENSION REDUCTION

For the A-B-A edges, since the crystal momentum, say q_y, along the edge is a still good quantum number, using the Fourier transform

$$\hat{a}^\dagger_{\mathbf{m}\sigma} = \frac{1}{\sqrt{N_y}}\sum_{q_y} e^{-iq_y n\tilde{d}}\hat{a}^\dagger_{n\sigma}(q_y),$$
$$\hat{b}^\dagger_{\mathbf{m}\sigma} = \frac{1}{\sqrt{N_y}}\sum_{q_y} e^{-iq_y n\tilde{d}}\hat{b}^\dagger_{n\sigma}(q_y) \tag{E1}$$

with N_y and $\tilde{d} = \sqrt{2}d$ being the number of the unit cells and the lattice spacing, respectively, along the edge, for each q_y a one-dimensional effective tight-binding model can be obtained as

$$\begin{aligned}\hat{h}(q_y) = \sum_{m\sigma}\{&[t\hat{a}^\dagger_{m\sigma}(q_y)\hat{b}_{m-1,\sigma}(q_y)\\ &+ te^{-iq_y\tilde{d}}\hat{a}^\dagger_{m\sigma}(q_y)\hat{b}_{m+1,\sigma}(q_y) + t(1+e^{-iq_y\tilde{d}})\hat{a}^\dagger_{m\sigma}\\ &\times(q_y)\hat{b}_{m\sigma}(q_y) + i\eta_\sigma t'\hat{a}^\dagger_{m\sigma}(q_y)\hat{b}_{m-1,\bar{\sigma}}(q_y)\\ &- i\eta_\sigma t'e^{-iq_y\tilde{d}}\hat{a}^\dagger_{m\sigma}(q_y)\hat{b}_{m+1,\bar{\sigma}}(q_y)\\ &+ t'(1-e^{-iq_y\tilde{d}})\hat{a}^\dagger_{m\sigma}(q_y)\hat{b}_{m\bar{\sigma}}(q_y) + \text{H.c.}]\\ &+ \eta_\sigma m_z[\hat{a}^\dagger_{m\sigma}(q_y)\hat{a}_{m\sigma}(q_y) + \hat{b}^\dagger_{m\sigma}(q_y)\hat{b}_{m\sigma}(q_y)]\},\end{aligned} \tag{E2}$$

where $\eta_\sigma = 1$ and -1 for $\sigma = \uparrow$ and $\downarrow$, respectively. By defining the new basis

$$\hat{s}_{m\pm}(q_y) \equiv \frac{1}{\sqrt{2}}[\hat{a}_{m\uparrow}(q_y) \pm e^{-iq_y\tilde{d}/2}\hat{b}_{m\uparrow}(q_y)],$$
$$\hat{p}_{m\pm}(q_y) \equiv \frac{1}{\sqrt{2}}[\hat{a}_{m\downarrow}(q_y) \mp e^{-iq_y\tilde{d}/2}\hat{b}_{m\downarrow}(q_y)], \tag{E3}$$

Eq. (E2) can also be block-diagonalized to Eq. (9), which corresponds to two 1D hybridized s-p models.

APPENDIX F: BREAKING NONSYMMORPHIC SYMMETRIES

Whereas in the main text we have focused on the lattice potential that respects the nonsymmorphic symmetry, it is useful to discuss perturbations that may break such a symmetry. To concretize our discussions, we focus on a perturbation potential

$$V' = \alpha \sin\frac{\pi(x-y)}{d}\sin\frac{\pi(x+y)}{d}, \tag{F1}$$

which opens up a finite gap δ at the zone boundary between the lowest two bands. Similar to other symmetry protected topological states, if δ is much smaller than relevant energy scales in the unperturbed system, it is expected that such perturbation will not change the results in the main text qualitatively. For instance, when $\delta \ll \Delta$, the exponentially small mixing with the higher bands is negligible, and one is allowed to focus on the Hilbert space spanned by the lowest two bands. The new eigenstates thus correspond to a unitary transformation of the unperturbed ones, which is denoted as U. Correspondingly, the non-Abelian Berry curvature, which is gauge dependent, becomes $\mathbf{F} \to U^\dagger\mathbf{F}U$. Nevertheless, the first Chern number is gauge independent, as the trace of

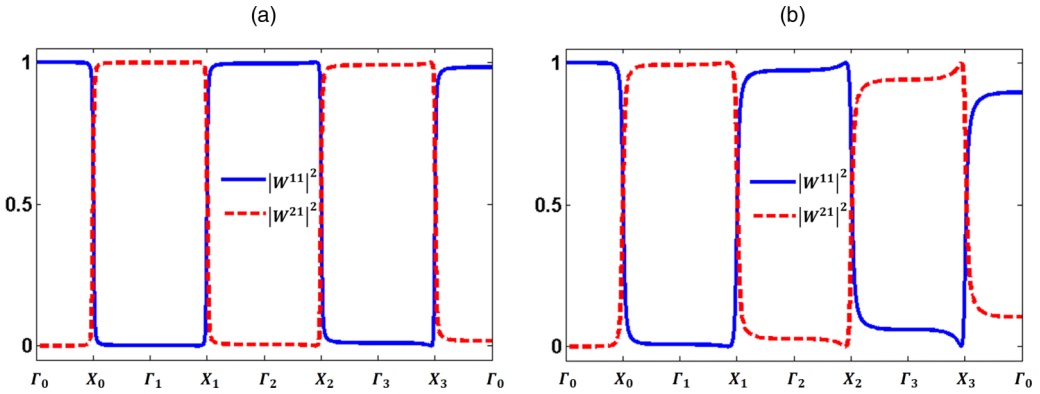

FIG. 7. Wilson lines after breaking the nonsymmorphic symmetry. Squared amplitudes of the two elements, W^{11} and W^{21}, of the Wilson loop denoted in Fig. 2(b) after breaking the nonsymmorphic symmetry with the energy offset (a) $\delta = 0.2t$ and (b) $\delta = 0.5t$, respectively. The other parameters of the tight-binding model are $t' = t, m_z = -3t$.

the tensor remains unchanged. Thus, the quantum charge pumping remains unaffected. It is worth mentioning that, when δ becomes finite, it is certainly allowed to use the Abelian Berry phase to compute the Chern number of each individual band separately. Interestingly, $C_1 + C_2 = C$, where C_1 and C_2 are the Chern numbers of the first and second bands computed from Abelian Berry curvature, respectively. Such an identity can be easily seen from $\mathbf{F}_1 + \mathbf{F}_2 = \mathrm{tr}(\mathbf{F})$, where $\mathbf{F}_{1(2)}$ is the Abelian Berry curvature for the first (second) band. We further consider tuning α in V', so that $\alpha = 0$ corresponds to a transition point, at which δ vanishes. On either side of the transition point, C_1 and C_2 are computed, and we find out that $C_1 + C_2$ is conserved, since $\mathbf{F}_1 + \mathbf{F}_2 = \mathrm{tr}(\mathbf{F})$ is satisfied on both sides of the transition point.

The corresponding tight-binding model with this perturbation is similar to Eq. (2), with only additional energy difference terms in the diagonal elements, yielding

$$H(\mathbf{k}) = \begin{pmatrix} m_z & \Omega_{\mathbf{k}} e^{i\theta_{\mathbf{k}}} & 0 & N_{\mathbf{k}} e^{i\theta_{\mathbf{k}}} \\ \Omega_{\mathbf{k}} e^{-i\theta_{\mathbf{k}}} & m_z + \delta & -N_{\mathbf{k}} e^{-i\theta_{\mathbf{k}}} & 0 \\ 0 & -N^*_{\mathbf{k}} e^{i\theta_{\mathbf{k}}} & -m_z & \Omega_{\mathbf{k}} e^{i\theta_{\mathbf{k}}} \\ N^*_{\mathbf{k}} e^{-i\theta_{\mathbf{k}}} & 0 & \Omega_{\mathbf{k}} e^{-i\theta_{\mathbf{k}}} & -m_z + \delta \end{pmatrix}. \tag{F2}$$

The definitions of the quantities are the same as those in the main text. For a small δ, as shown in Fig. 7, the qualitative result of the Wilson line remains unchanged, except for a quantitative difference that it is no longer a step function, but changes smoothly across the zone boundary, similar to the 1D system we considered recently [34]. We have also verified that the results of edge states of A-B-A edges also remain qualitatively the same, as shown in Fig. 8(a). Though the bulk states can no longer be labeled by the parity of the nonsymmorphic symmetry, such a label still works for the edge state, if its energy is well separated from the bulk by a finite gap such that the perturbation induced mixing between $\lambda = +$ and $\lambda = -$ is exponentially small for the edge state. Figure 8(b) shows $\tilde{\lambda} = \langle \phi_e | G_e | \phi_e \rangle / (i e^{i p_y \tilde{d}/2})$, where $|\phi_e\rangle$ is the edge state and G_e is the nonsymmorphic operator along the A-B-A edge, as a function of the momentum q_y. It is clear that $\tilde{\lambda}$ remains to be 1 or -1, with exponentially small corrections, unless the edge state begins to merge into the bulk states, or coupled to edge states with the opposite parity in a small system.

APPENDIX G: EVOLUTION FROM NODAL BOUNDARY TO NODAL LINE

One could also retain the nonsymmorphic symmetry but break the symmetries M_x or M_y, which, in general, can be realized by making the Hamiltonian Eq. (4) anisotropic along $x + y$ and $x - y$ directions. Thus, the potentials become

$$V(\mathbf{r}) = V_x \cos^2 \frac{\pi(x-y)}{d} + V_y \cos^2 \frac{\pi(x+y)}{d}, \tag{G1}$$

$$\Omega_x(\mathbf{r}) = \Omega_x \cos \frac{\pi(x-y)}{d} \sin \frac{\pi(x+y)}{d}, \tag{G2}$$

$$\Omega_y(\mathbf{r}) = -\Omega_y \sin \frac{\pi(x-y)}{d'} \cos \frac{\pi(x+y)}{d}. \tag{G3}$$

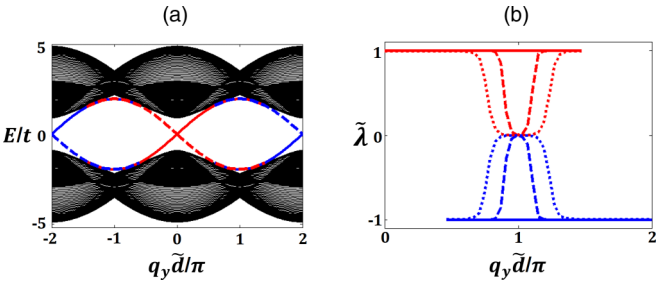

FIG. 8. Energy spectrum and the parities of the edge states after breaking nonsymmorphic symmetry. (a) Energy spectra with A-B-A boundaries after breaking the nonsymmorphic symmetry by $\delta = 0.2t$. The solid and dashed lines represent the edge states on the right and left boundaries, respectively. The nondegenerate parts with single red or blue colors represent $\tilde{\lambda} \simeq 1$ or -1, respectively, while for the overlapping parts of the red and blue curves the parity is not well defined. (b) The parity $\tilde{\lambda}$ of the $E/t > 0$ edge states for the $q_y > 0$ part with $\delta = 0$ (solid), $0.001t$ (dashed), and $0.1t$ (dotted). That of $q_y < 0$ is symmetric with respect to $q_y = 0$. The curves terminate when the edge states merge into the bulk. In the vicinity of $q_y\tilde{d} = \pm\pi$, edge states are strongly coupled to the bulk and those at the other side of the system such that the parity is not well defined, corresponding to the overlapping parts of the red and blue curves of edge states in (a). When $q_y\tilde{d} = 0$ and $\pm 2\pi$, edge states are separated from the bulk by a finite gap and the parity is thus well conserved. Other tight-binding model parameters used here are $t' = t, m_z = -t$.

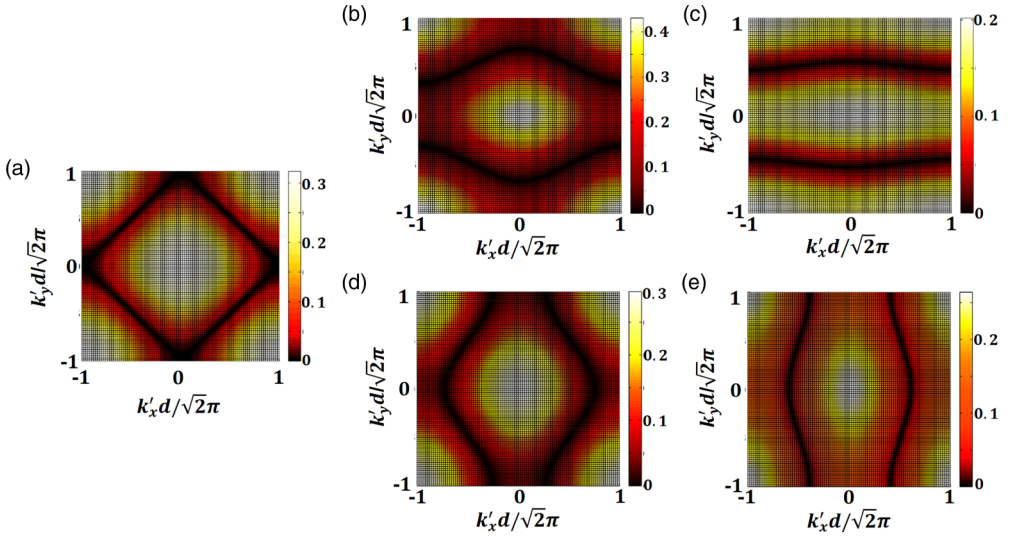

FIG. 9. Evolution of the nodal line. The contour plots are the energy difference of the lowest two bands by plane-wave expansions, and the black curves are the nodal lines. (a) The isotropic case with $(V_x, V_y) = (10,10)E_R$ and $(\Omega_x, \Omega_y) = (5,5)E_R$. (b,c) The anisotropy induced by the lattice potentials with $(V_x, V_y) = (10,8)E_R$ and $(\Omega_x, \Omega_y) = (5,5)E_R$, and $(V_x, V_y) = (10,0)E_R$ and $(\Omega_x, \Omega_y) = (5,5)E_R$, respectively. (d,e) The anisotropy induced by the Raman potentials with $(V_x, V_y) = (10,10)E_R$ and $(\Omega_x, \Omega_y) = (5,4)E_R$, and $(V_x, V_y) = (10,10)E_R$ and $(\Omega_x, \Omega_y) = (5,0)E_R$, respectively. All are with $m_z = -E_R$. $E_R = \hbar^2 k_0^2/2M$ is the recoil energy with $k_0 = \pi/d'$ and M being the mass of the atoms.

After M_x or M_y is broken, the nodal BZ boundary turns to a nodal line. As shown in Fig. 9, the nodal line deforms when changing the anisotropy of either the lattice potentials, $V_x \neq V_y$ [Figs. 9(a)–9(c)], or the Raman potentials, $\Omega_x \neq \Omega_y$ [Figs. 9(a), 9(d), and 9(e)]. The nodal line always exists because the nonsymmorphic symmetry, $G_{x\pm y}$, is preserved, though M_x and M_y are broken. Interestingly, as shown in Fig. 9, the nodal line always gets through the four X points, i.e., $\mathbf{k} = (0, \pm\pi/d), (\pm\pi/d, 0)$, no matter how anisotropic the system is. Actually, such band crossing points are protected by the inversion symmetry, I—$x \to d/2 - x, y \to -d/2 - y$—which, combined with the nonsymmorphic symmetry, ensures the four nodal X points in BZ. To see this, one notices the relation

$$IG_{x-y} = G_{x-y} IT(d, -d), \tag{G4}$$

where $T(d, -d)$ is the translation operator, which translates the state by d and $-d$ along x and y directions, respectively. For Bloch states, it becomes

$$IG_{x-y} = G_{x-y} I e^{i(k_x - k_y)d}, \tag{G5}$$

which shows, at X points, the inversion operator and the nonsymmorphic operator are anticommutative, so the degeneracy is guaranteed.

Our system thus provides physicists a highly controllable platform to create and manipulate the nodal lines in the momentum space.

[1] D. J. Thouless, M. Kohmoto, M. P. Nightingale, and M. den Nijs, Phys. Rev. Lett. **49**, 405 (1982).
[2] F. D. M. Haldane, Phys. Rev. Lett. **61**, 2015 (1988).
[3] M. Z. Hasan and C. L. Kane, Rev. Mod. Phys. **82**, 3045 (2010).
[4] D. Xiao, M.-C. Chang, and Q. Niu, Rev. Mod. Phys. **82**, 1959 (2010).
[5] X.-L. Qi and S.-C. Zhang, Rev. Mod. Phys. **83**, 1057 (2011).
[6] C. L. Kane and E. J. Mele, Phys. Rev. Lett. **95**, 146802 (2005).
[7] B. A. Bernevig, T. L. Hughes, and S.-C. Zhang, Science **314**, 1757 (2006).
[8] M. König, S. Wiedmann, C. Brüne, A. Roth, H. Buhmann, L. W. Molenkamp, X.-L. Qi, and S.-C. Zhang, Science **318**, 766 (2007).
[9] N. Regnault and B. A. Bernevig, Phys. Rev. X **1**, 021014 (2011).
[10] D. C. Tsui, H. L. Stormer, and A. C. Gossard, Phys. Rev. Lett. **48**, 1559 (1982).
[11] R. B. Laughlin, Phys. Rev. Lett. **50**, 1395 (1983).
[12] F. D. M. Haldane, Phys. Rev. Lett. **51**, 605 (1983).
[13] S. A. Trugman and S. Kivelson, Phys. Rev. B **31**, 5280 (1985).
[14] V. Galitski and I. B. Spielman, Nature (London) **494**, 49 (2013).
[15] I. B. Spielman, Ann. Phys. **525**, 797 (2013).
[16] M. Aidelsburger, M. Atala, M. Lohse, J. T. Barreiro, B. Paredes, and I. Bloch, Phys. Rev. Lett. **111**, 185301 (2013).
[17] H. Miyake, G. A. Siviloglou, C. J. Kennedy, W. C. Burton, and W. Ketterle, Phys. Rev. Lett. **111**, 185302 (2013).
[18] G. Jotzu, M. Messer, R. Desbuquois, M. Lebrat, T. Uehlinger, D. Greif, and T. Esslinger, Nature (London) **515**, 237 (2014).
[19] M. Atala, M. Aidelsburger, J. T. Barreiro, D. Abanin, T. Kitagawa, E. Demler, and I. Bloch, Nat. Phys. **9**, 795 (2013).
[20] M. Aidelsburger, M. Lohse, C. Schweizer, M. Atala, J. T. Barreiro, S. Nascimbene, N. R. Cooper, I. Bloch, and N. Goldman, Nat. Phys. **11**, 162 (2015).
[21] M. Lohse, C. Schweizer, O. Zilberberg, M. Aidelsburger, and I. Bloch, Nat. Phys. **12**, 350 (2016).
[22] S. Nakajima, T. Tomita, S. Taie, T. Ichinose, H. Ozawa, L. Wang, M. Troyer, and Y. Takahashi, Nat. Phys. **12**, 296 (2016).

[23] S. M. Young and C. L. Kane, Phys. Rev. Lett. **115**, 126803 (2015).
[24] C. Fang and L. Fu, Phys. Rev. B **91**, 161105 (2015).
[25] B. Bradlyn, J. Cano, Z. Wang, M. G. Vergniory, C. Felser, R. J. Cava, and B. A. Bernevig, Science **353**, aaf5037 (2016).
[26] A. Alexandradinata, Z. Wang, and B. A. Bernevig, Phys. Rev. X **6**, 021008 (2016).
[27] T. Bzduek, Q. Wu, A. Regg, M. Sigrist, and A. A. Soluyanov, Nature (London) **538**, 75 (2016).
[28] F. Wilczek and A. Zee, Phys. Rev. Lett. **52**, 2111 (1984).
[29] A. A. Burkov, M. D. Hook, and L. Balents, Phys. Rev. B **84**, 235126 (2011).
[30] H. Weng, Y. Liang, Q. Xu, R. Yu, Z. Fang, X. Dai, and Y. Kawazoe, Phys. Rev. B **92**, 045108 (2015).
[31] Z. Wu, L. Zhang, W. Sun, X.-T. Xu, B.-Z. Wang, S.-C. Ji, Y. Deng, S. Chen, X.-J. Liu, and J.-W. Pan, Science **354**, 83 (2016).
[32] K. Shiozaki, M. Sato, and K. Gomi, Phys. Rev. B **91**, 155120 (2015).
[33] Q.-Z. Wang and C.-X. Liu, Phys. Rev. B **93**, 020505 (2016).
[34] S.-L. Zhang and Q. Zhou, arXiv:1604.06292.
[35] D. Culcer, Y. Yao, and Q. Niu, Phys. Rev. B **72**, 085110 (2005).
[36] T. Li, L. Duca, M. Reitter, F. Grusdt, E. Demler, M. Endres, M. Schleier-Smith, I. Bloch, and U. Schneider, Science **352**, 1094 (2016).
[37] X. Li, E. Zhao, and W. Vincent Liu, Nat. Commun. **4**, 1523 (2013).
[38] W. Zheng and H. Zhai, Phys. Rev. A **89**, 061603 (2014).
[39] S.-L. Zhang and Q. Zhou, Phys. Rev. A **90**, 051601 (2014).
[40] P. Cladé, C. Ryu, A. Ramanathan, K. Helmerson, and W. D. Phillips, Phys. Rev. Lett. **102**, 170401 (2009).
[41] N. Navon, A. L. Gaunt, R. P. Smith, and Z. Hadzibabic, Science **347**, 167 (2015).